

# Dalton Transactions

Accepted Manuscript



This article can be cited before page numbers have been issued, to do this please use: V. Mahalingam, M. Chatti, K. N. K. B. Adusumalli and S. Ganguli, *Dalton Trans.*, 2016, DOI: 10.1039/C6DT02548J.



This is an *Accepted Manuscript*, which has been through the Royal Society of Chemistry peer review process and has been accepted for publication.

*Accepted Manuscripts* are published online shortly after acceptance, before technical editing, formatting and proof reading. Using this free service, authors can make their results available to the community, in citable form, before we publish the edited article. We will replace this *Accepted Manuscript* with the edited and formatted *Advance Article* as soon as it is available.

You can find more information about *Accepted Manuscripts* in the [Information for Authors](#).

Please note that technical editing may introduce minor changes to the text and/or graphics, which may alter content. The journal's standard [Terms & Conditions](#) and the [Ethical guidelines](#) still apply. In no event shall the Royal Society of Chemistry be held responsible for any errors or omissions in this *Accepted Manuscript* or any consequences arising from the use of any information it contains.

# Near-infrared light triggered superior photocatalytic activity from $\text{MoS}_2\text{-NaYF}_4\text{:Yb}^{3+}/\text{Er}^{3+}$ nanocomposites

Manjunath Chatti, Venkata N. K. B. Adusumalli, Sagar Ganguli and Venkataramanan Mahalingam<sup>\*a</sup>

<sup>a</sup> Department of Chemical Sciences, Indian Institute of Science Education and Research (IISER), Kolkata, Mohanpur, West Bengal, 741246, India.

**KEYWORDS:** Lanthanides, 2D materials, Nanocrystals, Energy transfer.

## **ABSTRACT:**

A near infrared (NIR) responsive photocatalyst, composed of narrow band gap semiconductor (i.e.  $\text{MoS}_2$ ) and an optical material possessing the upconverting ability (i.e.  $\text{NaYF}_4\text{:Yb}^{3+}/\text{Er}^{3+}$ ) has been successfully prepared via a simple hydrothermal method. The latter has the ability to convert the NIR light into visible ones while the  $\text{MoS}_2$  uses the light to degrade organic pollutants. Upon near infrared (NIR) excitation of the  $\text{MoS}_2\text{-NaYF}_4\text{:Yb}^{3+}/\text{Er}^{3+}$  nanocomposites, the energy of the strong green and the red emissions along with the weak violet emissions from the  $\text{NaYF}_4\text{:Yb}^{3+}/\text{Er}^{3+}$  nanocrystals (NCs) are transferred to  $\text{MoS}_2$ . This results in enhanced NIR light triggered photocatalytic performance as verified by studying the degradation of Rhodamine B (RhB) dye under 980 nm laser excitation. The strong photocatalytic activity of  $\text{MoS}_2\text{-NaYF}_4\text{:Yb}^{3+}/\text{Er}^{3+}$  composites is attributed to the layered nature of photocatalyst which

leads to efficient separation of photogenerated carriers (electron–hole pairs) and excellent upconversion properties of NaYF<sub>4</sub>:Yb<sup>3+</sup>/Er<sup>3+</sup> NCs. The study also shows the importance of the composite formation as the physical mixture lead to only very low photocatalytic activity. Our results can be helpful in the structural design and development of high-performance photocatalysts.

## INTRODUCTION

With increased development in science and technology, air and water pollution have become a major concern to the society. In an effort to control the pollution, environmentally friendly photocatalysis technique is applied in the degradation of organic pollutants in air and water. In past, considerable attention has been paid to semiconductor based photocatalysis for water treatment because of its efficient conversion of organic pollutants to environmentally friendly by products.<sup>1-4</sup> Generally, the overall photocatalytic performance of semiconductors are mainly decided by three factors: (1) The adsorption ability of photocatalyst, (2) the separation and migration rate of the photogenerated carriers (holes and electrons) to the surface of catalyst, and (3) photoabsorption ability in the available light energy region.<sup>5</sup> Desired photocatalysts are expected to satisfy aforementioned factors. Considering the above factors, the traditional photocatalysts, such as TiO<sub>2</sub> and ZnO with wide band gap can only exhibit high photocatalytic activity under ultraviolet light irradiation. This significantly limits their practical applications<sup>6-8</sup> as it is well known that UV light covers only about 5% of the solar spectrum. On the other hand the visible light and near-infrared (NIR) light occupy significant portion of the solar spectrum i.e. 49% and 46%, respectively.<sup>9</sup> Therefore, development of a photocatalyst for efficient sunlight harvesting is a challenge.<sup>10</sup> Furthermore, smaller sphere shaped

nanoparticles are generally preferred as photocatalysts due to higher specific surface area. But latter's photocatalytic activity is significantly affected by higher electron-hole recombination rate.<sup>11</sup> Recent studies have demonstrated that the geometry of photocatalyst has a significant effect on the photocatalytic activity.<sup>12</sup>

In recent past, photocatalysis using 2D materials has attracted researchers around the world and has become one of the interesting research topics.<sup>13-15</sup> 2D layered materials possess two main intrinsic advantages which can be utilized to enhance the photocatalytic efficiency. First, 2D materials maximize the surface area availability per amount of material for photocatalytic reactions. Second, due to 2D nature the distance that photogenerated carriers (electrons and holes) have to migrate will be less thereby reducing the possible recombination of electron-hole and potentially enhancing the photocatalytic performance. Among various 2D materials MoS<sub>2</sub> is quite interesting and widely studied. MoS<sub>2</sub>, being inorganic graphene analogue, consists of molybdenum atoms sandwiched between two layers of hexagonally close-packed sulfur atoms.<sup>16-19</sup> MoS<sub>2</sub> with a narrow band gap of 1.8 eV has strong absorption in the visible region of solar spectrum; therefore it has been explored for photocatalytic applications.<sup>20-24</sup> Although, there are quite a few reports on visible light photocatalysts, research efforts on NIR driven photocatalytic activities are still in the early stage.

Recently, there have been few reports on NIR light triggered photocatalysts developed by integrating semiconductors with upconversion (UC) nanocrystals. The latter possess the ability to convert NIR photons to visible photons.<sup>25-37</sup> Moreover the long luminescence lifetime of the lanthanide ions ensures the efficient energy transfer to semiconductors. For example, Weiping et al developed NIR driven TiO<sub>2</sub> and ZnO based photocatalysts by preparing YF<sub>3</sub>:Yb<sup>3+</sup>/Tm<sup>3+</sup>@TiO<sub>2</sub>,<sup>38</sup> NaYF<sub>4</sub>:Yb<sup>3+</sup>/Tm<sup>3+</sup>@TiO<sub>2</sub><sup>39</sup> core/shell nanoparticles and

NaYF<sub>4</sub>:Yb<sup>3+</sup>/Tm<sup>3+</sup>@ZnO<sup>40</sup> nanocomposites, respectively. However, because of the larger band gap of aforementioned semiconductors only a small amount of weak upconverted UV light can be harvested under NIR irradiation rather than stronger visible emissions. To our knowledge there are only few reports where researchers have developed composites which can harvest the upconverted visible light.<sup>41-44</sup> For instance, Li *et al.* have recently reported the NIR driven photocatalytic activity of NaYF<sub>4</sub>:Yb<sup>3+</sup>,Er<sup>3+</sup>/CdS composite.<sup>41</sup> Similarly, Guo *et al* have reported the NIR assisted photocatalysis by NaYF<sub>4</sub>:Yb<sup>3+</sup>,Er<sup>3+</sup>/CdS/TiO<sub>2</sub> composite, which is able to degrade about 90% of MB in 50 hours.<sup>42</sup> In another work, enhanced NIR driven photocatalytic activity was observed from  $\beta$ -NaYF<sub>4</sub>:Yb<sup>3+</sup>,Tm<sup>3+</sup>/g-C<sub>3</sub>N<sub>4</sub> nanocomposite.<sup>44</sup> Our idea is to integrate UC NCs with layered narrow band gap semiconductor MoS<sub>2</sub> to efficiently utilize the upconverted visible emissions. One of the advantages of using MoS<sub>2</sub> is the broad absorption in the visible region thus can efficiently use the unconverted emissions.

In this work, we report the NIR light triggered photocatalytic activity of MoS<sub>2</sub>-NaYF<sub>4</sub>:Yb<sup>3+</sup>/Er<sup>3+</sup> nanocomposites prepared using hydrothermal method. The energy of intense green and red emissions along with weak upconverted UV emission from UC NCs are efficiently transferred to the MoS<sub>2</sub>. This resulted in enhanced NIR light triggered photocatalytic activity of MoS<sub>2</sub> which is verified by monitoring the degradation of Rhodamine B (RhB) dye. The degradation of dye occurs much faster compared to other reports in the literature. These results pave way to the structural design of new type of NIR active catalytic materials.

## EXPERIMENTAL SECTION

### *Chemicals and Materials:*

All the chemicals used in this work such as yttrium oxide ( $\text{Y}_2\text{O}_3$ , 99.99%), ytterbium oxide ( $\text{Yb}_2\text{O}_3$ , 99.99%), erbium oxide ( $\text{Er}_2\text{O}_3$ , 99.99%) were purchased from Sigma Aldrich. Adipic acid (AA) (90%), ammonium heptamolybdate, thiourea, sodium fluoride (NaF), nitric acid ( $\text{HNO}_3$ ), and absolute ethanol were purchased from Merck. All the materials were used without further purification. Lanthanide nitrates were prepared by mixing appropriate amount of corresponding oxides with conc.  $\text{HNO}_3$  and the residual  $\text{HNO}_3$  was removed by evaporation.

### *Synthesis:*

***Synthesis of adipic acid coated  $\text{NaYF}_4:\text{Yb}^{3+}/\text{Er}^{3+}$  nanocrystals:***  $\text{NaYF}_4:\text{Yb}^{3+}/\text{Er}^{3+}$  NCs were synthesized via high temperature hydrothermal method. Briefly,  $\text{Ln}(\text{NO}_3)_3$ , ( $\text{Ln}$ : 78 mol%  $\text{Y}^{3+}$ , 20 mol%  $\text{Yb}^{3+}$ , 2 mol%  $\text{Er}^{3+}$ ) were dissolved in 15 mL distilled water and then 15 mL ethanol was added to above aqueous solution under magnetic stirring. Then 8 mmol NaF and 4 mmol of adipic acid were added into the above solution. The mixture was stirred for about 30 minutes before transferred to a 50 mL autoclave, sealed, and hydrothermally treated at  $200^\circ\text{C}$  for 24 h. The system was cooled to room temperature naturally, and the products were deposited at the bottom of the vessel. Pure powders could be obtained by purifying the samples with ethanol several times to remove excess NaF.

***Synthesis of  $\text{MoS}_2$ :***  $\text{MoS}_2$  nanosheets were synthesized via hydrothermal method, similar to those previously reported. Briefly, to a beaker containing 15 mL water appropriate amount of ammonium heptamolybdate and thiourea was added and stirred for 30 minutes. The clear transparent solution was subsequently transferred into a teflon lined autoclave and heated at  $220^\circ\text{C}$  for 24 h. Subsequently, the reaction system was allowed to cool to room temperature. As

a final step the product was collected by means of centrifugation, washed twice with ethanol, and once with deionized water.

**Synthesis of  $\text{MoS}_2\text{-NaYF}_4\text{:Yb}^{3+}/\text{Er}^{3+}$  nanocomposites:** Hydrothermal synthesis technique was adopted for the synthesis of  $\text{MoS}_2\text{-NaYF}_4\text{:Yb}^{3+}/\text{Er}^{3+}$  nanocomposites. In a typical procedure, 50 mg of  $\text{MoS}_2$  was dispersed well in 15 mL of water via sonication. To the above dispersion  $\text{Ln}(\text{NO}_3)_3$ , ( $\text{Ln}$ : 78 mol%  $\text{Y}^{3+}$ , 20 mol%  $\text{Yb}^{3+}$ , 2 mol%  $\text{Er}^{3+}$ ) were added and stirred for 30 minutes followed by addition of 15 mL of ethanol. Then 8 mmol NaF and 4 mmol of adipic acid were added into the above solution. The mixture was stirred for about 1 h, then transferred to a 50 mL autoclave, sealed, and hydrothermally treated at 200°C for 24 h. The system was cooled to room-temperature naturally, and the products deposited at the bottom of the vessel were purified with ethanol several times to remove excess NaF.

**Photocatalytic activity evaluation:** The photocatalytic activity of the composites was evaluated by studying the degradation of Rhodamine B (RhB) under near-infrared (NIR) light irradiation by a 980 nm diode laser source from RGB Lase LLC. In each experiment, 20 mg of sample was dispersed into a quartz vial containing 10 mL RhB solution (25 mg  $\text{L}^{-1}$ ). Prior to irradiation, the suspensions were stirred in dark for 1 hour to reach adsorption-desorption equilibrium. Subsequently, the colloidal dispersion was exposed to NIR light irradiation inside a closed black chamber with continuous magnetic stirring. At each irradiation time interval, 1 mL aliquot of the suspension containing the photocatalyst and RhB solution was collected and centrifuged (6500 rpm, 5 minutes) to remove the photocatalyst particles in order to assess rate of degradation photometrically. The colloidal dispersion was analyzed by a Hitachi UV-4100 UV-vis-NIR spectrophotometer, and the characteristic absorption of RhB at 554 nm was used to monitor the photocatalytic degradation. All the measurements were carried out at room temperature.

**Photogenerated hydroxyl radical ( $\cdot\text{OH}$ ) detection:** 4 mM terephthalic acid (TA) solution was prepared in 2 mM NaOH solution. To 10 mL TA solution, 20 mg of photocatalyst was added and dispersed thoroughly via sonication. The resulting mixture was then irradiated with 980 nm laser and after certain interval, 1.0 mL of suspensions were collected and centrifuged. For the photoluminescence measurement, 0.5 mL of as collected dispersion was diluted five times. The generation of 2-hydroxyterephthalic (TAOH) acid was monitored using fluorescence spectrophotometer with an excitation wavelength of 312 nm.

### Characterization techniques:

The crystallinity and phase analysis of the nanomaterials were carried out using powder X-ray diffraction (PXRD) measurements using a Rigaku-Smart lab diffractometer with Cu-K $\alpha$  operating at 70 kV and 35 mA at a scanning rate of 1° per minute in the range of 10-90°. The samples were completely powdered and spread evenly on a quartz slide. The morphology of the nanomaterials was characterized by scanning electron microscopy (SEM). SEM images were taken using a ZEISS (SUPRA) instrument and for this the samples dispersed in ethanol were drop casted on a silicon wafer and further coated with a thin film of gold/platinum to avoid charging effects prior to loading of the samples into the chamber. The FTIR spectra were recorded using Perkin Elmer RX1 spectrophotometer with KBr disk technique operating in the range of 4000-400 cm<sup>-1</sup>. For recording the FTIR spectra 10 mg of the samples were mixed with 200 mg of KBr to make the pellets. The photoluminescence measurement was performed using Horiba Jobin Yvon Fluorolog spectrophotometer equipped with 450 W Xe lamp. The PL lifetime measurements were performed with a Horiba Jobin Yvon Fluorolog CP machine equipped with a pulsed Xe source operating at 25 W. The upconversion emission (UC) measurements were done by exciting the dispersion of the nanocrystals using a 980 nm diode laser source from RGB Lase



LLC, which was coupled with a fiber with core diameter of 100  $\mu\text{m}$ . The output signal was measured with the Horiba Jobin Yvon Fluorolog spectrophotometer. BET surface area measurements were carried out by  $\text{N}_2$  adsorption at 77.3 K using a Quantachrome Novawin2 instrument. All the measurements were performed at room temperature. Zeta potential measurements were carried out on a Malvern Zetasizer Nano instrument equipped with a 4.0 mW He–Ne laser operating at  $\lambda=633$  nm.

## RESULTS AND DISCUSSIONS:

*Phase analysis:* The crystal structure and phase purity of the samples were characterized by PXRD. Figure 1 (a) shows the PXRD pattern of the  $\text{MoS}_2$  sample prepared via hydrothermal route and can be readily indexed to the hexagonal phase of  $\text{MoS}_2$  which is consistent with the standard powder diffraction pattern of  $\text{MoS}_2$  (JCPDS 37-1492) shown in Figure 1 (b). The typical XRD patterns of the  $\text{MoS}_2\text{-NaYF}_4\text{:Yb}^{3+}/\text{Er}^{3+}$  nanocomposites and  $\text{NaYF}_4\text{:Yb}^{3+}/\text{Er}^{3+}$  NCs are shown in Figure 1 (c and d) respectively. For  $\text{NaYF}_4\text{:Yb}^{3+}/\text{Er}^{3+}$  NCs, the diffraction peaks were well-defined, the peak positions and intensities agreed well with standard cubic pattern of  $\text{NaYF}_4$  (PDF card No. 01-077-2042) shown in Figure 1 (e), indicating that the as-prepared  $\text{NaYF}_4\text{:Yb}^{3+}/\text{Er}^{3+}$  NCs material is pure and crystallize in cubic phase. Figure 1 (c) shows XRD pattern of  $\text{MoS}_2\text{-NaYF}_4\text{:Yb}^{3+}/\text{Er}^{3+}$  nanocomposites obtained via one-pot hydrothermal route. The sample showed the characteristic peaks of  $\text{NaYF}_4\text{:Yb}^{3+}/\text{Er}^{3+}$  NCs but it is worth to mention that the appearance of a weak diffraction peak (see Figure c1) at  $2\theta = 14.4^\circ$ . This peak is assigned to the (002) plane of  $\text{MoS}_2$  which supports the presence of  $\text{MoS}_2$  in  $\text{MoS}_2\text{-NaYF}_4\text{:Yb}^{3+}/\text{Er}^{3+}$  nanocomposites. The weak intensity of  $\text{MoS}_2$  peaks is due to the presence of small amount of  $\text{MoS}_2$  in the nanocomposites.

*Morphology analysis:* High resolution scanning electron microscopy was used for morphology and size analysis of the as synthesized samples. FE-SEM images shown in Figure 2 (a) illustrate that the adipic acid capped  $\text{NaYF}_4:\text{Yb}^{3+}/\text{Er}^{3+}$  NCs are spherical in morphology. The average particle size of the  $\text{NaYF}_4:\text{Yb}^{3+}/\text{Er}^{3+}$  NCs is approximately 40 nm. The SEM images of  $\text{MoS}_2$  shown in Figure 2 (b) indicate the formation of cauliflower like morphology. At a closer look it is clear that  $\text{MoS}_2$  nanostructure is composed of nanowalls of about several nanometers in thickness.<sup>45</sup> For the  $\text{MoS}_2\text{-NaYF}_4:\text{Yb}^{3+}/\text{Er}^{3+}$  nanocomposites changes in the roughness of  $\text{MoS}_2$  nanostructures upon deposition of  $\text{NaYF}_4$  nanocrystals on  $\text{MoS}_2$  nanostructures can be clearly observed in the FESEM images shown in Figure 2 (c). We believe during the initial growth of the nanocomposite, the cations attach on the negatively charged  $\text{MoS}_2$  nanosheets through electrostatic interactions. The presumption is supported by the observed zeta potential value of -19 mV for  $\text{MoS}_2$  nanosheets. The nanosheets then act as a nucleation site for the growth of the NCs. This suggests the successful formation of the  $\text{MoS}_2\text{-NaYF}_4:\text{Yb}^{3+}/\text{Er}^{3+}$  nanocomposites. The EDX spectral results shown in Figure 2 (d) further confirm the presence of elements (such as Mo, S, Na, Y, F, Yb and Er) in the nanocomposites. The photoluminescence measurements of the resulting products provide further evidence of formation of  $\text{MoS}_2\text{-NaYF}_4:\text{Yb}^{3+}/\text{Er}^{3+}$  composites. (*vide infra*)

*Surface functionalization-FTIR analysis:* The attachment of adipic acid molecules onto the surface of the nanocrystals is confirmed from Fourier transform infrared (FTIR) analysis. The FTIR spectra of adipic acid capped  $\text{NaYF}_4:\text{Yb}^{3+}/\text{Er}^{3+}$  NCs and  $\text{MoS}_2\text{-NaYF}_4:\text{Yb}^{3+}/\text{Er}^{3+}$  nanocomposites along with pure adipic acid are shown in Figure S1. All the IR absorption bands of the main functional groups present in the adipic acid are observed. In case of  $\text{NaYF}_4$  nanocrystals and  $\text{MoS}_2\text{-NaYF}_4:\text{Yb}^{3+}/\text{Er}^{3+}$  nanocomposites a weak peak near  $1565\text{ cm}^{-1}$  due to

carbonyl stretching is observed. This stretching frequency is much lower than the  $1708\text{ cm}^{-1}$  observed for the free adipic acid molecules, implying the binding of the O-atom of the -COOH group of adipic acid to the surface of the nanocrystals. The binding of adipic acid molecules to the nanocrystals makes the nanocrystals surface hydrophilic to disperse them in polar solvents.

*UV-vis-NIR absorption properties:* Figure 3, shows the UV-Vis spectrum of  $\text{MoS}_2$ . Three absorption peaks at 450, 624 and 670 nm are observed for  $\text{MoS}_2$  which show the semiconducting nature of  $\text{MoS}_2$ . The two characteristic absorption peaks at 624 nm (1.99 eV) and 670 nm (1.85 eV) arise from direct transition from valance band to conduction band at the K-point of the Brillouin zone, known as the B and A transitions, respectively. The little energy difference between the two peaks is because of the spin-orbital splitting of the valence band. In addition, the broad absorption band centered at 450 nm (2.75 eV) arising from the complicated C and D transitions is also observed.<sup>46-50</sup> In the inset of Figure 4, the absorption spectra of (a)  $\text{MoS}_2$ - $\text{NaYF}_4:\text{Yb}^{3+}/\text{Er}^{3+}$  nanocomposites and (b) pure  $\text{NaYF}_4:\text{Yb}^{3+}/\text{Er}^{3+}$  NCs; the characteristic absorption peaks between 400-700 nm corresponding to  $\text{MoS}_2$  are observed. The observed weak UV-Vis absorption of  $\text{MoS}_2$  in the nanocomposites is due to the low amount of  $\text{MoS}_2$  loading.

*Upconversion (UC) luminescence properties:* The UC emission spectrum of adipic acid encapsulated  $\text{Yb}^{3+}$ (20%)/ $\text{Er}^{3+}$ (2%)-doped  $\text{NaYF}_4$  NCs upon excitation with a 980 nm continuous wave (CW) diode laser is shown in Figure 4 (a), where  $\text{Yb}^{3+}$  serves as sensitizer and  $\text{Er}^{3+}$  acts as activator. Four major bands are observed around 408, 523 nm, 545 nm, and 655 nm in the UC emission spectrum. The intense green emissions appearing close to 520 and 545 nm are assigned to the  $^2\text{H}_{11/2} \rightarrow ^4\text{I}_{15/2}$  and  $^4\text{S}_{3/2} \rightarrow ^4\text{I}_{15/2}$  transitions in  $\text{Er}^{3+}$ , respectively. The strong emission peak appearing in the red region is assigned to transition occurring between the  $^4\text{F}_{9/2}$  and  $^4\text{I}_{15/2}$  levels of  $\text{Er}^{3+}$ . The violet emission (408 nm) and UV emission (379 nm) are ascribed to the  $^2\text{H}_{9/2} \rightarrow ^4\text{I}_{15/2}$

and  $^4G_{11/2} \rightarrow ^4I_{15/2}$  transitions of  $\text{Er}^{3+}$  ions, respectively. The involvement of two 980 nm photons in providing both green and red emission is verified by performing power dependent studies as the UC emission intensity (I) is directly proportional to  $n^{\text{th}}$  power of laser power (P),  $I \propto P^n$ . A plot of  $\ln(I)$  versus  $\ln(P)$  for both green and red emissions of the  $\text{NaYF}_4:\text{Yb}^{3+}/\text{Er}^{3+}$  NCs along with the resulting slope values are shown in Figure S2. The calculated values are 1.58 and 1.33 for 545 nm and 650 nm emissions of  $\text{NaYF}_4:\text{Yb}^{3+}/\text{Er}^{3+}$  NCs, respectively. The above values clearly suggest the participation of two 980 nm photons in producing both green and red emissions. These values are lower than the expected value of 2 due to saturation of the UC process.<sup>51</sup> The possible energy transfer mechanism between  $\text{Yb}^{3+}$  and  $\text{Er}^{3+}$  is shown in Figure S3, using the energy level diagram of  $\text{Yb}^{3+}$  and  $\text{Er}^{3+}$  ions. Figure 4 (c) indicates a drastic decrease in the observed upconversion emission intensity for  $\text{MoS}_2\text{-NaYF}_4:\text{Yb}^{3+}/\text{Er}^{3+}$  nanocomposites. We believe this strong quenching of the upconverted fluorescence of  $\text{NaYF}_4:\text{Yb}^{3+}/\text{Er}^{3+}$  NCs is likely due to  $\text{MoS}_2$ . This is reasonable because  $\text{MoS}_2$  has strong absorption over wide wavelength region (350 to 700 nm) as shown in Figure 3. This covers the fluorescence emission regions of  $\text{NaYF}_4:\text{Yb}^{3+}/\text{Er}^{3+}$  NCs. In order to understand whether the reduction in the UC luminescence intensity is due to energy transfer or rather due to radiation-reabsorption, we performed a control experiment. A physical mixture of  $\text{MoS}_2$  and  $\text{NaYF}_4:\text{Yb}^{3+}/\text{Er}^{3+}$  NCs was prepared by taking the same molar ratio as that in the nanocomposite. The mixture was grinded well and their UC properties were studied. The mixture shows intense UC upon excitation at 980 nm and the extent of reduction in the upconversion emission intensity is much less compared to that noted for the nanocomposites. This suggests that the observed decrease in the intensity of the UC emission intensity for the nanocomposites is likely due to high energy transfer from the excited  $\text{Er}^{3+}$  ions to  $\text{MoS}_2$  in the nanocomposites. To further understand the quenching mechanism, lifetime

measurements were performed (as shown in Figure S4). The lifetime curves were obtained by the direct excitation of the  $\text{Er}^{3+}$  ions at an excitation wavelength of 488 nm. The significant decrease in the decay time of  $\text{Er}^{3+}$  ions in nanocomposites (8  $\mu\text{s}$ ) compared to that in the  $\text{NaYF}_4:\text{Yb}^{3+}/\text{Er}^{3+}$  NCs alone (40  $\mu\text{s}$ ) indicates the energy migration between  $\text{NaYF}_4:\text{Yb}^{3+}/\text{Er}^{3+}$  NCs and  $\text{MoS}_2$  is a resonance energy transfer (RET) process, rather than a radiation–reabsorption process or charge transfer process. The latter is a difficult process to occur as the redox potentials of many of the lanthanide ions are high. Especially, it is worth to mention that the difference in the energy transfer efficiency from  $\text{Er}^{3+}$  to  $\text{MoS}_2$  affects the NIR photocatalytic activity of  $\text{MoS}_2$  significantly, which will be discussed in the photocatalytic activity section. (*vide infra*)

*Photocatalytic study:* The photocatalytic performance of the  $\text{MoS}_2\text{-NaYF}_4:\text{Yb}^{3+}/\text{Er}^{3+}$  nanocomposites was evaluated by studying the degradation of Rhodamine B (RhB) dye under 980 nm NIR irradiation. 20 mg of the  $\text{MoS}_2\text{-NaYF}_4:\text{Yb}^{3+}/\text{Er}^{3+}$  nanocomposites were dispersed into a quartz vial containing 10 mL of RhB aqueous solution. In order to know the actual amount of RhB decomposed via photocatalysis, the dark reaction of RhB in the presence of catalysts was conducted to establish the adsorption/desorption equilibrium of RhB on the surfaces of the  $\text{MoS}_2\text{-NaYF}_4:\text{Yb}^{3+}/\text{Er}^{3+}$  nanocomposites. As can be seen from Figure 5, the nanocomposite adsorbs about 37.5% of RhB after 1 hour in dark condition. Thereafter, the solution was subjected to NIR irradiation and 1 mL of RhB aqueous solution was taken out for UV-vis absorption measurement after regular intervals of 1 hour. This high adsorption of dye molecules on the composite photocatalyst may be ascribed to the 2D nature of  $\text{MoS}_2$  nanosheets. In comparison to nanoparticles, 2D nanosheets are known to possess large surface area, which in turn is able to adsorb significantly more dye molecules than nanoparticles. Moreover,

photocatalytic activity of a material largely depends on the extent of adsorption by the photocatalyst. Hence, both high adsorption and large surface area assist in the photocatalysis process as well. We believe the nature of adsorption of pollutants on photocatalyst surfaces follow the Langmuir theory, which postulated that adsorption is monolayer and excess molecules are reflected back from the surfaces.<sup>52</sup> It has been earlier reported that photogenerated oxidizing species are not able to migrate far from the photocatalysts and the degradation process occurs at the surface or within a few monolayers around the photocatalytic particles.<sup>53</sup>

Figure 5 shows the absorbance spectra of RhB loaded  $\text{MoS}_2\text{-NaYF}_4\text{:Yb}^{3+}/\text{Er}^{3+}$  nanocomposites under NIR irradiation as a function of the irradiation time. The observed gradual decrease in the absorption intensity of RhB at 554 nm with the increase in the irradiation time clearly indicates the degradation of RhB upon the NIR irradiation. Figure 6 shows the time-dependent profile of  $C/C_0$  (degradation ratio), where  $C$  is the concentration of RhB irradiated with a 980 nm laser for time  $t$  and  $C_0$  is the original concentration of RhB after attaining adsorption equilibrium with the photocatalysts well before irradiation. From Figure 6 (d), it is clear that the degradation ratio of RhB is observed to increase continuously with the irradiation time and reached about 61% after 12 h irradiation in the presence of  $\text{MoS}_2\text{-NaYF}_4\text{:Yb}^{3+}/\text{Er}^{3+}$  nanocomposites. The observed degradation rate is much higher compared to the other upconversion photocatalysts (see Table S1 in supporting information). We strongly believe the observed faster degradation is due to the layered nature of  $\text{MoS}_2$  and excellent upconversion properties of NCs. The surface area of a photocatalyst plays important role behind its activity. Thus, BET surface area measurements were carried out, which clearly indicate there is not much change in the surface area of  $\text{MoS}_2$  in the composite ( $10.74 \text{ m}^2\text{g}^{-1}$ ) upon deposition of  $\text{NaYF}_4\text{:Yb}^{3+}/\text{Er}^{3+}$  NCs compared to  $\text{MoS}_2$  alone ( $13.78 \text{ m}^2\text{g}^{-1}$ ). Furthermore, to know the difference in the photocatalytic ability of  $\text{MoS}_2\text{-}$

NaYF<sub>4</sub>:Yb<sup>3+</sup>/Er<sup>3+</sup> nanocomposites and the NaYF<sub>4</sub>-Yb/Er/ MoS<sub>2</sub> physical mixture, the latter was mixed with RhB solution and irradiated with NIR light for 12 h. Interestingly, only 18% of the RhB was found to be decomposed, which is almost over three times lower than that observed for MoS<sub>2</sub>-NaYF<sub>4</sub>:Yb<sup>3+</sup>/Er<sup>3+</sup> nanocomposites (61%). We attribute this to the difference in their energy migration pathways, as has been discussed in the upconversion section. In the nanocomposites structure, NaYF<sub>4</sub>:Yb<sup>3+</sup>/Er<sup>3+</sup> NCs and MoS<sub>2</sub> are attached closely with each other and form compact interfaces, this benefits energy transfer processes as the distance between MoS<sub>2</sub> and UC nanoparticles are within energy transfer distance. In contrast, we believe there are no contact interfaces between NaYF<sub>4</sub>-Yb/Er and MoS<sub>2</sub> nanomaterials in the physical mixture, and thus, MoS<sub>2</sub> can be excited mainly via radiation-reabsorption. However, in the MoS<sub>2</sub>-NaYF<sub>4</sub>:Yb<sup>3+</sup>/Er<sup>3+</sup> nanocomposites, more NIR photon energy have been used to activate MoS<sub>2</sub> leading to relatively higher photocatalytic activity. These results indicate that energy transfer plays an important mechanism in the NIR photocatalytic activity. Moreover, NaYF<sub>4</sub>:Yb<sup>3+</sup>/Er<sup>3+</sup> NCs and MoS<sub>2</sub> alone showed limited photocatalytic activities for degradation of RhB. It is also well established in the literature that the thermal energy generated by NIR irradiation is not sufficient enough to induce the thermal degradation of RhB.<sup>41</sup>

It is essential to understand the origin of the degradation of RhB under irradiation of 980 nm NIR laser in the presence of MoS<sub>2</sub>-NaYF<sub>4</sub>:Yb<sup>3+</sup>/Er<sup>3+</sup> nanocomposites. In most of the cases, it is the reactive oxygen species like hydroxyl radicals ( $\cdot$ OH) are considered to be responsible for degradation of organic contaminants because of their strong oxidation ability. To confirm the generation of  $\cdot$ OH during the photocatalytic process of MoS<sub>2</sub>-NaYF<sub>4</sub>:Yb<sup>3+</sup>/Er<sup>3+</sup> nanocomposites under NIR irradiation, we used terephthalic acid (TA) as a fluorescence probe to measure  $\cdot$ OH generation. The nonfluorescent TA captures  $\cdot$ OH to form hydroxyterephthalic acid (TAOH),

which shows fluorescence at 424 nm upon excitation at 312 nm UV light. Therefore, the formation of TAOH as well as the generation of  $\cdot\text{OH}$  can be selectively detected by monitoring the emission intensity at 424 nm. Figure 7 (a) shows photoluminescence spectra for the supernatant solution of the photocatalyst suspension containing 4 mM TA irradiated with 980 nm NIR laser for designated time. The collected spectra are characteristic of the fluorescence of TAOH, which indicates that  $\cdot\text{OH}$  is being produced during the NIR photocatalytic reactions. Moreover, the increased intensity with irradiation time indicates the increase in  $\cdot\text{OH}$  generation. Figure 7 (b), shows the time-dependent evolution of the fluorescence intensity of TAOH in the presence of different photocatalysts. The rate of generation of  $\cdot\text{OH}$  can be evaluated by the slope of the curve in Figure 7 (b). It is clear from this figure that upon NIR irradiation, almost no  $\cdot\text{OH}$  was generated in the case of only  $\text{MoS}_2$  and  $\text{NaYF}_4:\text{Yb}^{3+}/\text{Er}^{3+}$  NCs suggesting hardly any degradation of organic species occurs in the presence of these materials. On the other hand, in the presence of  $\text{MoS}_2\text{-NaYF}_4:\text{Yb}^{3+}/\text{Er}^{3+}$  composites,  $\cdot\text{OH}$  radicals were produced upon NIR irradiation. These results indicate that the energy transfer efficiency between  $\text{NaYF}_4:\text{Yb}^{3+}/\text{Er}^{3+}$  NCs and  $\text{MoS}_2$  is the key to cause the NIR photocatalytic activity.

*Photocatalysis Mechanism:* Scheme 1 describes the overall processes involved in the photocatalysis by the  $\text{MoS}_2\text{-NaYF}_4:\text{Yb}^{3+}/\text{Er}^{3+}$  nanocomposites under irradiation of 980 nm NIR laser. It mainly involves three processes i.e. (1) the formation of the excited states of  $\text{Er}^{3+}$ , (2) the activation of semiconductor via energy transfer, and (3) the generation of reactive oxygen species. Upon 980 nm excitation, the higher energy levels of the  $\text{Er}^{3+}$  ions ( $^4\text{I}_{11/2}$ ,  $^4\text{F}_{9/2}$  and  $^4\text{H}_{9/2}$ ) are populated via a successive energy transfer processes from  $\text{Yb}^{3+}$  to  $\text{Er}^{3+}$ . The semiconductor  $\text{MoS}_2$  is excited by the energy transfer from upconverting luminescent  $\text{NaYF}_4:\text{Yb}^{3+}/\text{Er}^{3+}$  NCs. Thus,  $\text{MoS}_2$  is activated to produce photogenerated carriers, that is, electrons and holes in the



conduction band (CB) and the valence band (VB), respectively (see Scheme 1). These electron-hole pairs migrate from the inner region to the surfaces to take part in surface reactions. As shown in Scheme 1, the excited electrons arriving on the surfaces react with the oxygen adsorbed on the surfaces of MoS<sub>2</sub> to form superoxide radical anion (O<sub>2</sub><sup>•-</sup>), whereas the photogenerated strongly oxidative holes (h<sup>+</sup>) react with H<sub>2</sub>O to produce hydroxyl radicals (•OH), which is considered as the main contributor for the degradation of RhB dye.

## Conclusions

In summary, adipic acid encapsulated NaYF<sub>4</sub>:Yb<sup>3+</sup>/Er<sup>3+</sup> upconversion nanocrystals were synthesized successfully by a hydrothermal method. The as synthesized NCs possess strong UC emission in the visible and UV region of solar spectrum. The potentiality of UC nanocrystals to absorb the NIR light in solar spectrum is utilized to enhance the photocatalytic performance of MoS<sub>2</sub>. The strong NIR driven photocatalytic capability of MoS<sub>2</sub>-NaYF<sub>4</sub>-Yb<sup>3+</sup>/Er<sup>3+</sup> upconversion photocatalyst is demonstrated via the degradation of RhB dye. Further, comparative studies performed between the MoS<sub>2</sub> - NaYF<sub>4</sub>:Yb<sup>3+</sup>/Er<sup>3+</sup> composites and the physical mixture of MoS<sub>2</sub> and NaYF<sub>4</sub>:Yb<sup>3+</sup>/Er<sup>3+</sup> NCs revealed the presence of different energy transfer pathways in the nanocomposites and the mixture which resulted in a large difference in the NIR driven photocatalytic activities. In addition, a series of control experiments revealed that the hydroxyl radicals are responsible for Rhodamine B (RhB) dye degradation under NIR irradiation. In conclusion, we have developed a facile method to synthesize MoS<sub>2</sub>-NaYF<sub>4</sub>:Yb<sup>3+</sup>/Er<sup>3+</sup> nanocomposites that combine the advantages of both MoS<sub>2</sub> and upconversion nanoparticles which can be used for applications beyond photocatalysis such as for broadband optical limiting applications, optoelectronic devices, etc.

## ASSOCIATED CONTENT

Supporting Information. FTIR spectra, lifetime, power dependent plot, energy transfer mechanism, “This material is available free of charge via the Internet at <http://pubs.acs.org>.”

## AUTHOR INFORMATION

### Corresponding Author

\* Fax: 91-33-25873020; Tel: +91(0)9007603474; E-mail: [mvenkataramanan@yahoo.com](mailto:mvenkataramanan@yahoo.com)

## ACKNOWLEDGMENT

VM thanks the Department of Science and Technology (DST) India, CSIR and IISER-Kolkata for the funding. MC thanks KVPY for his scholarship. VNKBA and SG thank UGC and CSIR, respectively, for their scholarship.

## REFERENCES

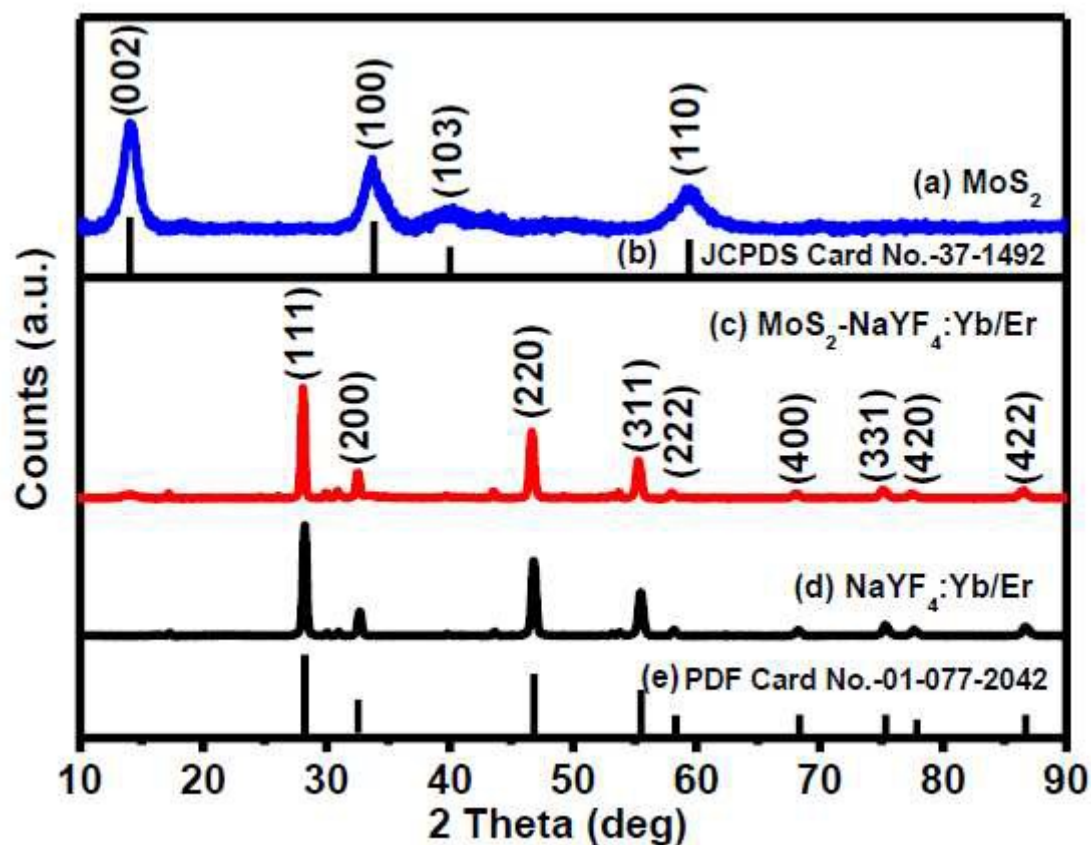
- (1) X. Bai, L. Wang, R. Zong, Y. Lv, Y. Sun and Y. Zhu. *Langmuir*, **2013**, 29, 3097–3105.
- (2) W. Yao, B. Zhang, C. Huang, C. Ma, X. Song and Q. Xu. *J. Mater. Chem.*, **2012**, 22, 4050–4055.
- (3) S. Higashimoto, Y. Tanaka, R. Ishikawa, S. Hasegawa, M. Azuma, H. Ohue and Y. Sakata. *Catal. Sci. Technol.*, **2013**, 3, 400–403.
- (4) Y. Wang, Z. Wang, S. Muhammad and J. He. *CrystEngComm*, **2012**, 14, 5065–5070.
- (5) Z. Ai, L. Zhang, S. Lee and W. Ho. *J. Phys. Chem. C*, **2009**, 113, 20896–20902.
- (6) X. J. Liu, L. K. Pan, T. Lv, Z. Sun and C. Q. Sun. *J. Colloid Interface Sci.*, **2013**, 408, 145–150.

- (7) X. J. Liu, L. K. Pan, T. Lv, T. Lu, G. Zhu, Z. Sun and C. Q. Sun. Microwave-assisted synthesis of ZnO–graphene composite for photocatalytic reduction of Cr(VI). *Catal. Sci. Technol.*, **2011**, *1*, 1189-1193.
- (8) T. Kamegawa, S. Matsuura, H. Seto and H. Yamashita. *Angew. Chem., Int. Ed.*, **2013**, *52*, 916-919.
- (9) W. P. Qin, D. S. Zhang, D. Zhao, L. L. Wang, K. Z. Zheng. *Chem. Commun.* **2010**, *46*, 2304–2306.
- (10) M. Anpo and M. Takeuchi. *Int. J. Photoenergy*, **2001**, *3*, 89– 94.
- (11) M. A. Grela, J. A. Colussi. *J. Phys. Chem.* **1996**, *100*, 18214-18221.
- (12) G. K. Mor, K. Shankar, M. Paulose, C. A. Grimes. *Nano Lett.* **2005**, *5*, 191-195.
- (13) B. Luo, G. Liu, L. Wang. *Nanoscale*, **2016**, *13*(8), 6904–6920.
- (14) F. Dong, L. Wu, Y. Sun, M. Fu, Z. Wu and S. C. Lee. *J. Mater. Chem.*, **2011**, *21*, 15171.
- (15) J. Hong, Y. Wang, W. Zhang and R. Xu.. *ChemSusChem*, **2013**, *6*, 2263-2268.
- (16). Venkata Subbaiah, Y. P.; K. J. Saji, K. J.; Tiwari, A. *Adv. Funct. Mater.* **2016**, *26*(13), 2046-2069.
- (17) M. Chhowalla, H. S. Shin, G. Eda, L.-J. Li, K. P. Loh and H. Zhang. *Nature Chem.*, **2013**, *5*, 263-275.
- (18) C. Tana and H. Zhang. *Chem. Soc. Rev.*, **2015**, *44*, 2713-2731.
- (19) J. Kibsgaard, Z. Chen, B. N. Reinecke and T. F. Jaramillo. *Nature Mater.*, **2012**, *11*, 963–969.

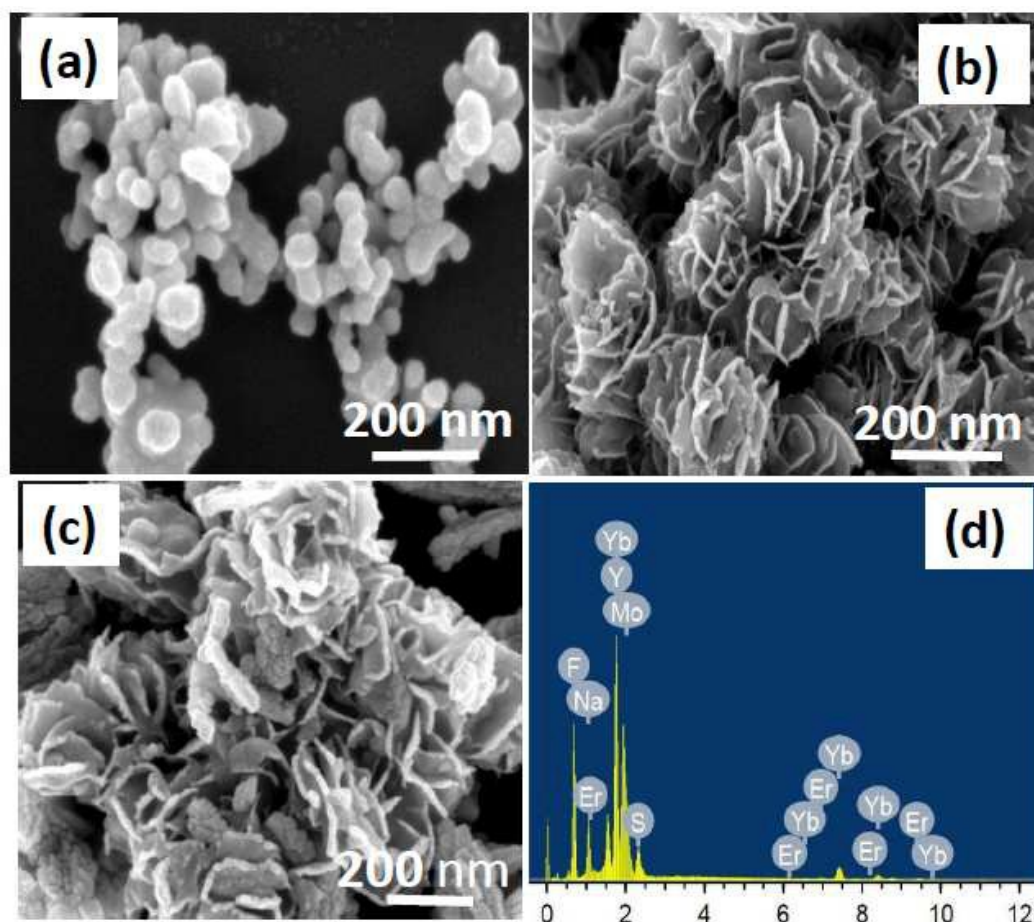
- (20) J. Li, K. Yu, Y. Tan, H. Fu, Q. Zhang, W. Cong, C. Song, H. Yin and Z. Zhu. *Dalton Trans.*, **2014**, *43*, 13136-13144.
- (21) F. A. Frame and F. E. Osterloh. *J. Phys. Chem. C*, **2010**, *114*, 10628–10633.
- (22) L. A. King, W. Zhao, M. Chhowalla, D. J. Riley and G. Eda. *J. Mater. Chem. A*, **2013**, *1*, 8935–8941.
- (23) Y. Li, Y. Li, C. M. Araujo, W. Luo and R. Ahuja. *Catal. Sci. Technol.*, **2013**, *3*, 2214–2220.
- (24) B. Visic, R. Dominko, M. K. Gunde, N. Hauptman, S. D. Skapin and M. Remskar. *Nanoscale Res. Lett.*, **2011**, *6*, 1–6.
- (25) S. Sivakumar, F. C. J. M. van Veggel and P. S. May. *J. Am. Chem. Soc.*, **2007**, *129*, 620–625.
- (26) F. Wang, X. J. Xue and X. Liu. *Angew. Chem., Int. Ed.*, **2008**, *47*, 906–909.
- (27) F. Wang, Y. Han, C. S. Lim, Y. Lu, J. Wang, J. Xu, H. Chen, C. Zhang, M. Hong, and X. Liu. *Nature*, **2010**, *463*, 1061-1065.
- (28) M. Haase and H. Schäfer. *Angew. Chem. Int. Ed.*, **2011**, *50*, 5808-5829.
- (29) O. Ehlert, R. Thomann, M. Darbandi and T. Nann. *ACS Nano*, **2008**, *2*, 120-124.
- (30) J.-C. G. Bünzli. *Chem. Rev.*, **2010**, *110*, 2729-2755.
- (31) X. Zhang, P. Yang, Y. Dai, P. Ma, X. Li, Z. Cheng, Z. Hou, X. Kang, C. Li, J. Lin. *Adv. Funct. Mater.* **2013**, *23*, 4067–4078.
- (32) J. de Wild, A. Meijerink, J. K. Rath, W. G. J. H. M. van Sark and R. E. I. Schropp. *Energy Environ. Sci.*, **2011**, *4*, 4835–4848.

- (33) S. Sarkar, B. Meeseragandla, C. Hazra and V. Mahalingam. *Adv. Mater.*, **2013**, 25, 856–860.
- (34) C. Boyer, F. Vetrone, L. A. Cuccia, J. A. Capobianco. *J. Am. Chem. Soc.* **2006**, 128, 7444–7445.
- (35) D. K. Chatterjee, M. K. Gnanasammandhan, Y. Zhang. *Small*, 2010, 6, 2781–2795.
- (36) M. Quintanilla, I. X. Cantarelli, M. Pedroni, A. Speghini and Vetrone. *J. Mater. Chem. C*, **2015**, 3, 3108–3113.
- (37) J. C. Boyer, N. J. J. Johnson, F. C. J. M. van Veggel. *Chem. Mater.*, **2009**, 21, 2010–2012.
- (38) W. Qin, D. Zhang, D. Zhao, L. Wanga and K. Zhenga. *Chem. Commun.*, **2010**, 46, 2304–2306.
- (39) Y. Tang, W. Di, X. Zhai, R. Yang and W. Qin. *ACS Catal.* **2013**, 3, 405–412.
- (40) X. Guo, W. Song, C. Chen, W. Di and W. Qin. *Phys. Chem. Chem. Phys.*, **2013**, 15, 14681–14688.
- (41) C. Li, F. Wang, J. Zhu and J. C. Yu. *Applied Catalysis B: Environmental.*, **2010**, 100, 433–449.
- (42) X. Guo, W. Di, C. Chen, C. Liu, X. Wang and W. Qin. *Dalton Trans.*, **2014**, 43, 1048–1054.
- (43) Q. C. Xu, Y. Zhang, M. J. Tan, Y. Liu, S. Yuan, C. Choong, N. S. Tan and T. T. Y. Tan. *Adv. Healthc. Mater.*, **2012**, 1, 470–474.
- (44) M-Z. Huang, B. Yuan, L. Dai and M-L. Fu., *J. Colloid Interface Sci.*, **2015**, 460, 264–272.
- (45) M. Chhowalla, H. S. Shin, G. Eda, L.-J. Li, K. P. Loh and H. Zhang. *Nature Chem.*, 2013, 5, 263–275.
- (46) K. F. Mak, K. He, C. Lee, G. H. Lee, J. Hone, T. F. Heinz, J. Shan. *Nature Mater.*, **2013**, 12, 207–211.

- (47) A. Splendiani, L. Sun, Y. Zhang, T. Li, J. Kim, C.-Y. Chim, G. Galli, F. Wang. *Nano Lett.*, **2010**, *10*, 1271-1275.
- (48) N. Bogdan, F. Vetrone, G. A. Ozin, J. A. Capobianco. *Nano Lett.* **2011**, *11*, 835-840.
- (49) G. Eda, H. Yamaguchi, D. Voiry, T. Fujita, M. Chen, M. Chhowalla. *Nano Lett.*, **2011**, *11*, 5111-5116.
- (50) A. O'Neill, U. Khan, J. N. Coleman. *Chem. Mater.*, **2012**, *24*, 2414-2421.
- (51) M. Pollnau, D. R. Gamelin, S. R. Luthi, H. U. Gudel and M. P. Hehlen. *Phys. Rev. B.*, **2000**, *61*, 3337-3346.
- (52) U. Gaya. *Heterogeneous photocatalysis using Inorganic semiconductor solids*. Page 75, Section 3.2.
- (53) C. Minero, F. Catozzo, E. Pelizzetti. *Langmuir*, **1992**, *8*, 481-486.

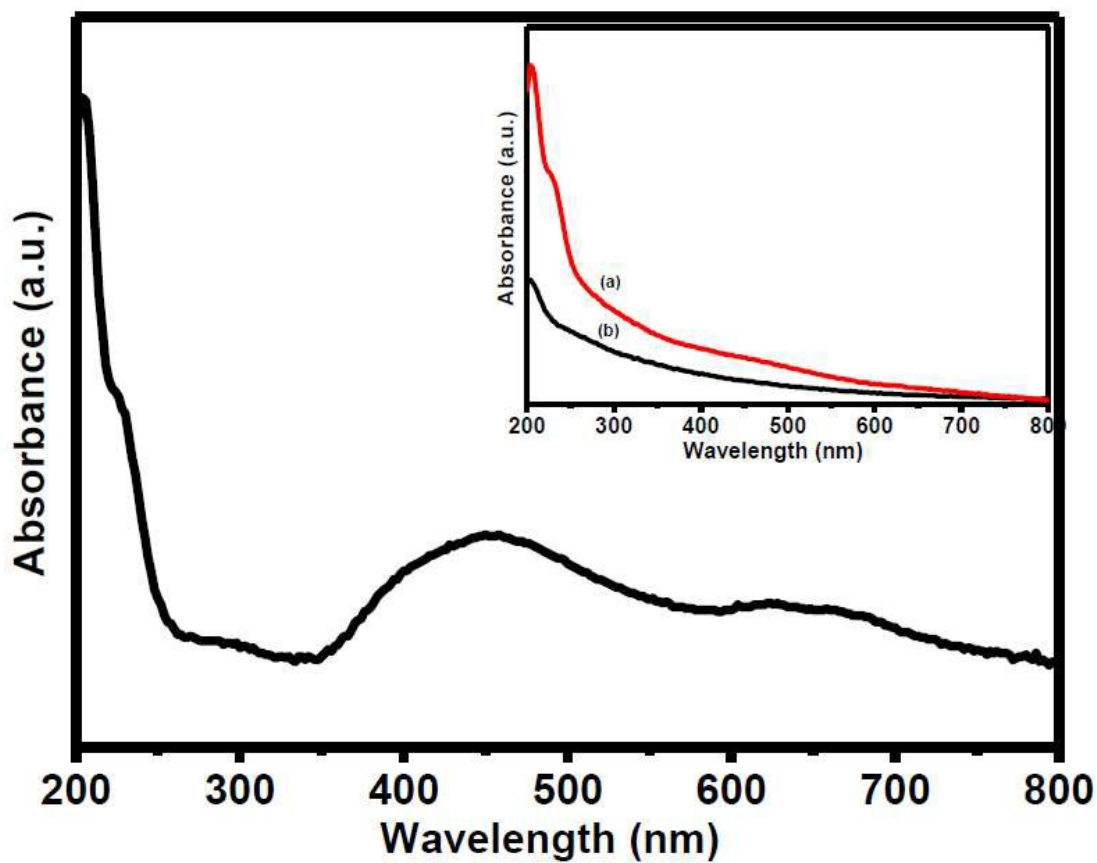


**Figure.1** XRD patterns of (a) MoS<sub>2</sub>, (c) MoS<sub>2</sub>-NaYF<sub>4</sub>:Yb<sup>3+</sup>/Er<sup>3+</sup> (d) NaYF<sub>4</sub>:Yb<sup>3+</sup>/Er<sup>3+</sup> nanomaterials and (b and e) standard XRD patterns of MoS<sub>2</sub> and bulk NaYF<sub>4</sub>.

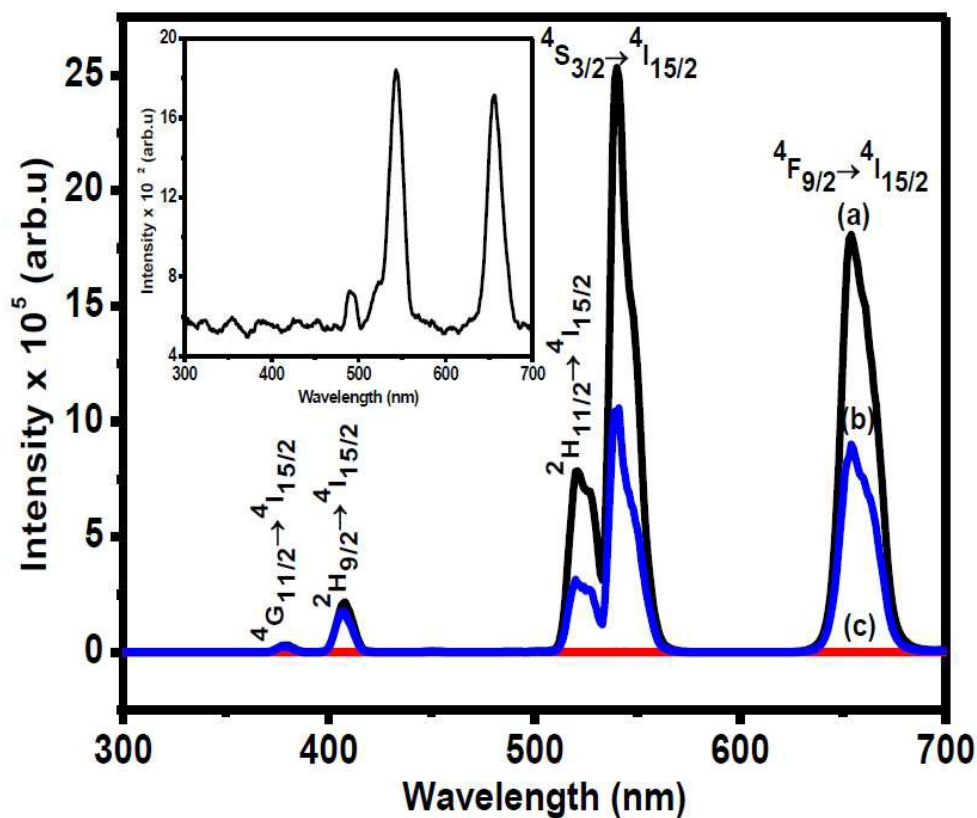


**Figure.2** FE-SEM images of (a) NaYF<sub>4</sub>:Yb<sup>3+</sup>/Er<sup>3+</sup> NCs, (b) MoS<sub>2</sub> and (c) MoS<sub>2</sub>-NaYF<sub>4</sub>:Yb<sup>3+</sup>/Er<sup>3+</sup> nanocomposites. EDX spectrum of (d) MoS<sub>2</sub>-NaYF<sub>4</sub>:Yb<sup>3+</sup>/Er<sup>3+</sup> nanocomposites.

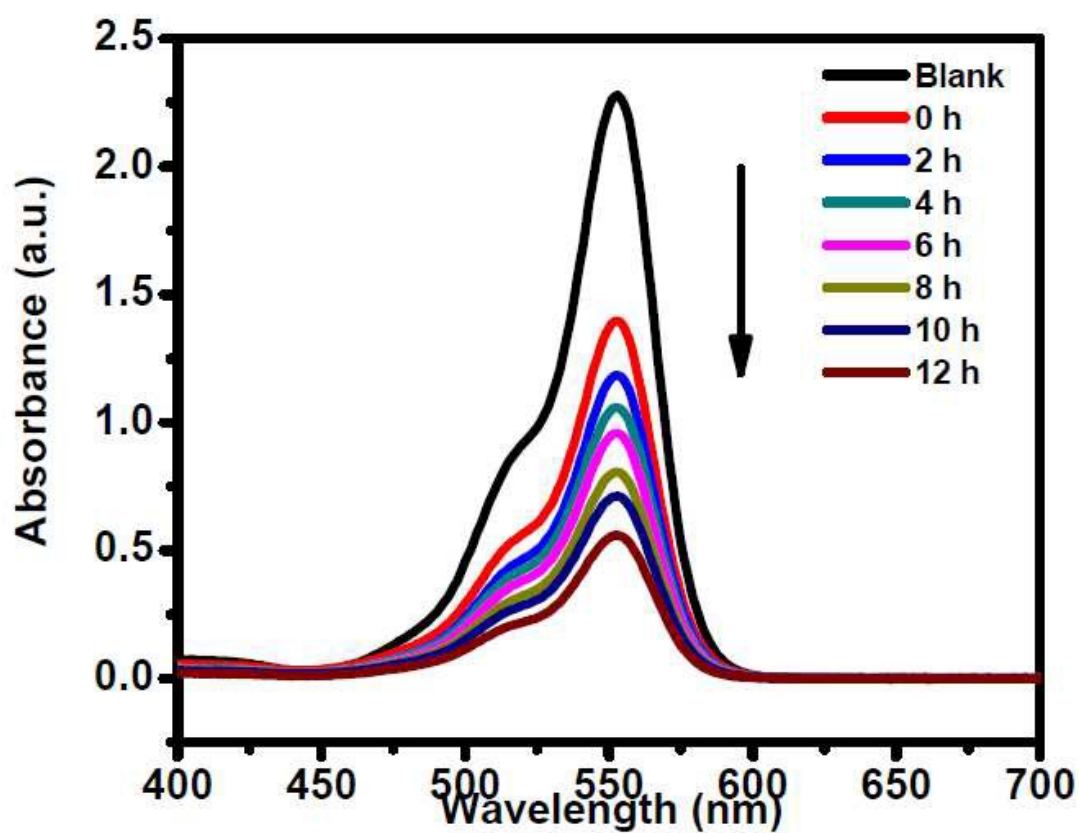




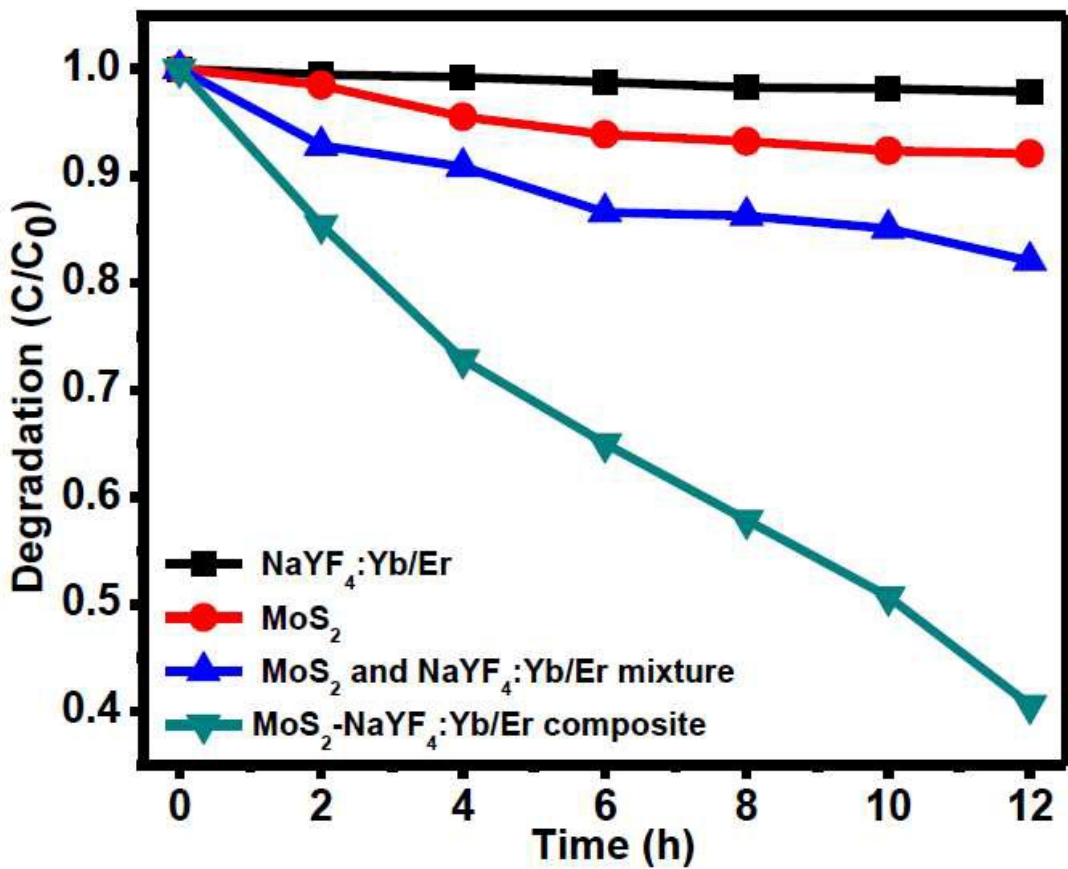
**Figure. 3.** UV-Vis absorption spectrum of MoS<sub>2</sub>. Inset shows the UV-Vis absorption spectra of (a) MoS<sub>2</sub>-NaYF<sub>4</sub>:Yb<sup>3+</sup>/Er<sup>3+</sup> nanocomposite (red curve) and (b) NaYF<sub>4</sub>:Yb<sup>3+</sup>/Er<sup>3+</sup> (black curve).



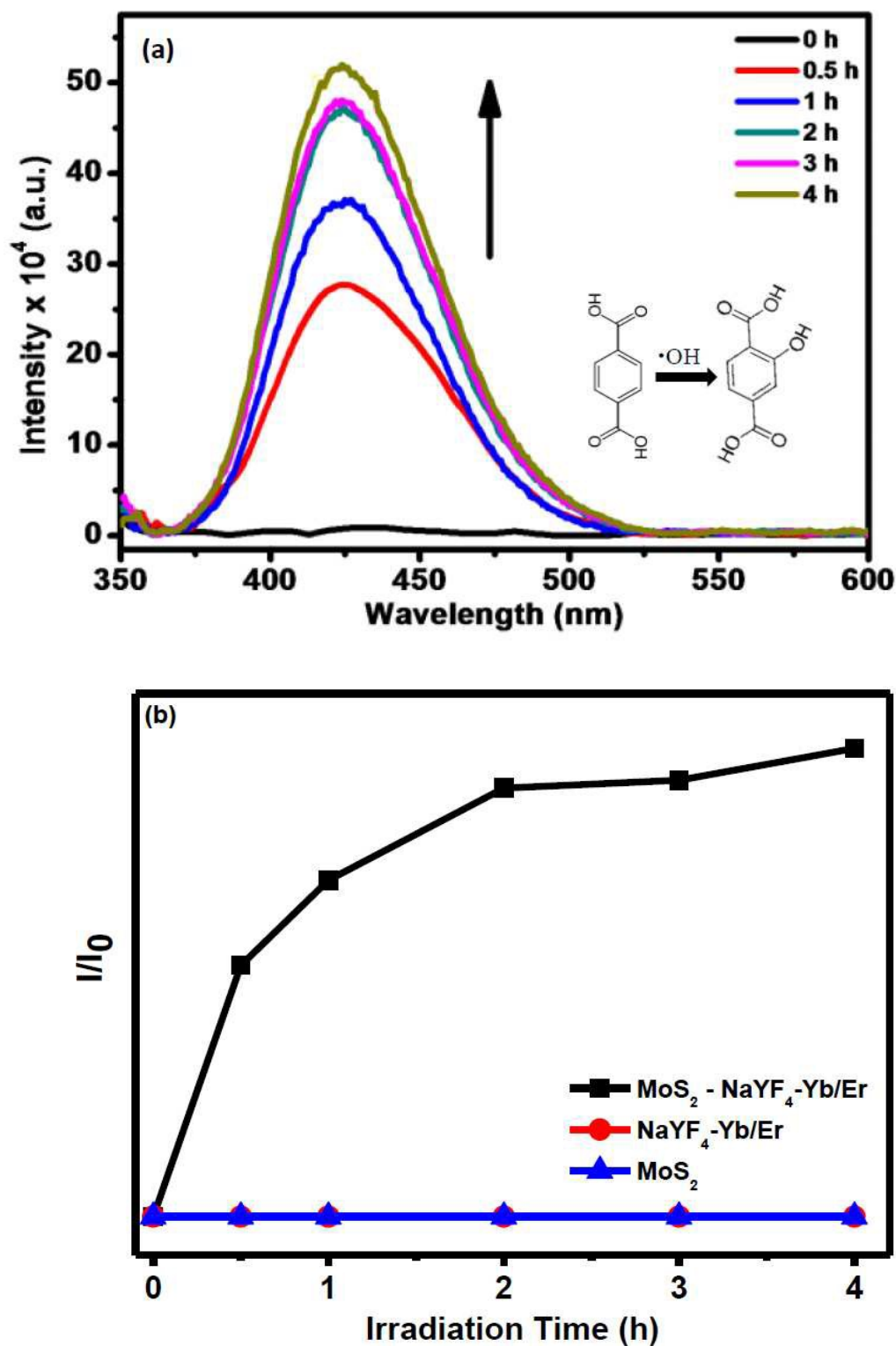
**Figure. 4.** The UC emission spectra of (a)  $\text{NaYF}_4:\text{Yb}^{3+}/\text{Er}^{3+}$  NCs (b) physical mixture of  $\text{NaYF}_4:\text{Yb}^{3+}/\text{Er}^{3+}$  NCs and  $\text{MoS}_2$  and (c)  $\text{MoS}_2\text{-NaYF}_4:\text{Yb}^{3+}/\text{Er}^{3+}$  composites (magnified spectrum shown in the inset) under 980 nm excitation.



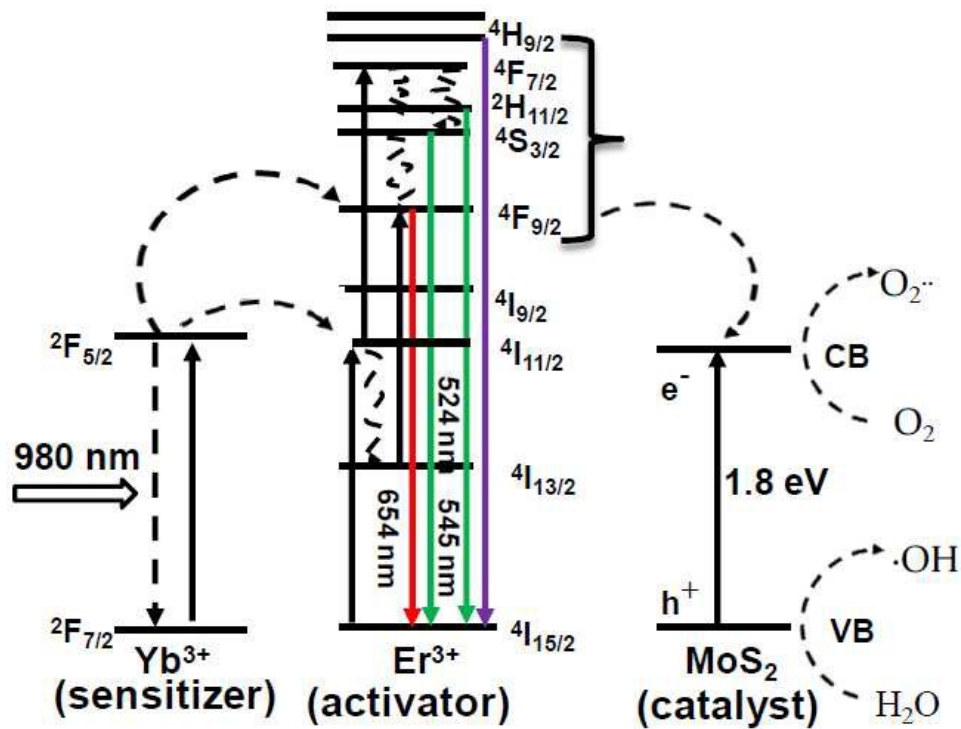
**Figure. 5** Temporal evolution of the absorbance spectra of RhB degradation under NIR irradiation in the presence of MoS<sub>2</sub>-NaYF<sub>4</sub>:Yb<sup>3+</sup>/Er<sup>3+</sup> nanocomposites.



**Figure. 6** The photocatalytic degradation rates of RhB under NIR irradiation for different photocatalyst solutions.



**Fig. 7** (a) Emission spectra of terephthalic acid (TA) solution and (b) fluorescence intensity ratio of the emission peak of TAOH at 420 nm as a function of time upon irradiation with 980 nm laser in the presence of MoS<sub>2</sub>-NaYF<sub>4</sub>-Yb/Er nanocomposite.



**Scheme 1.** Schematic illustration of near-infrared activated photocatalysis in MoS<sub>2</sub>-NaYF<sub>4</sub>:Yb<sup>3+</sup>/Er<sup>3+</sup> nanocomposites.